Scattering-matrix method for ballistic electron transport: Theory and an application to quantum antidot arrays

Hongqi Xu
Department of Solid State Physics, University of Lund, Box 118, S-221 00 Lund, Sweden
(Received 1 November 1993; revised manuscript received 6 June 1994)

In this paper we present a scattering-matrix formalism to study electron transport in a mesoscopic system such as a lateral antidot array with a strong modulation potential. We show that the physically important and less localized states are allowed to dominate in the implementation of the formalism and, therefore, the problem of the numerical instability that one often encounters in the application of the transfer-matrix method to lateral electron transport has been solved. As an example of its application, the formalism is used to calculate the electron transmission in one-dimensional (1D) antidot arrays defined in a narrow two-dimensional electron-gas (2DEG) constriction. We show that when the modulation potential of antidots is weak the conductance bands can appear at the edges of the conductance plateaus of the narrow 2DEG constriction. In the case of strong modulation the calculated conductance of the 1D antidot arrays are seen to be characterized by two kinds of strong fluctuations, namely, the slow and rapid fluctuations, in high Fermi-energy range. The slow fluctuations result from wave interferences and the formation of the electron minigaps in the arrays and are insensitive to the temperature up to a few Kelvin, while the rapid fluctuations reflect the formation of the electron minibands and can be easily smoothed out by thermal averaging. Due to strong overlaps between the minibands associated with different 1D paths in the strongly modulated antidot arrays, the effects of the regular miniband formation may only be observed in the low Fermi-energy range, even at very low temperature.

I. INTRODUCTION

It has been expected that in a lateral superlattice defined by a periodic potential in the plane of a two-dimensional electron gas (2DEG), minigaps of zero density of states and minibands may form if the potential varies periodically in one or both directions.[1] These lateral superlattice effects may be studied in the linear-response regime of a small applied voltage by varying the Fermi energy (E_F) or the strength of the periodic potential by means of a gate voltage. The conductance is expected to vanish if E_F is in a minigap. The experimental observations of this minigap effect in such two-dimensional (2D) lateral superlattices were reported first by Ismail *et al.*[2] and then by Smith *et al.*[3] However, no conclusive observations of the miniband structure of 2D lateral superlattices have been reported. This has been argued as being due to the difficulty in distinguishing between the true miniband effect and the quantum interference effect within a single unit cell.[1] The miniband structure has, however, been observed in a one-dimensional (1D) quantum-dot superlattice realized by means of patterned split-gate technique.[4]

With use of the transfer-matrix method, a number of exact quantum-mechanical calculations[5–10] have been made for ballistic transport through 1D lateral superlattices. However, only weakly modulated structures have been considered so far. The reason is that the transfer-matrix method is numerically unstable for systems involving strong modulations (e.g., strong antidot scatters, open quantum dots in large sizes, etc.). The origin of the failure can be traced to the coexistence of the exponentially growing and decaying waves as a result of including evanescent states in the formulations as demanded by completeness.

In this paper, we present an alternative formalism for treating electron transport in lateral quantum systems, based on the scattering matrices.[11] Previously, a scattering-matrix formalism was presented by Ko and Inkson[12] for multilayered semiconductor heterostructures where (effective) electron potential varies only in one dimension along the growth direction. The method proved to be numerically stable in the calculations of resonant tunneling in $GaAs/Al_xGa_{1-x}As$ multilayer systems.[12] However, the method has not been applied to electron transport in laterally patterned and/or confined structures for which the problems have to be formulated in two or three dimensions. Therefore, the power of the method has not been justified for the systems other than 1D cases. The purpose of this work is to generalize the method to electron transport in multidimensional structures and to explore the numerical power of the method in the calculations for more complicated quantum systems. In the present paper, we will mainly consider the generalization of the method to laterally patterned and confined 2DEG systems.

In what follows, we first give a general scattering-matrix formulation for electron transport in a lateral quantum system. Based on this formulation, we then show explicitly that the physically important states are allowed to dominate in the calculations, and the method remains numerically stable and accurate even in the limit of strong modulations and consisting of a large number of quantum dots and antidots with large sizes. As an exam-

ple of its application, we present the results of the calculations for ballistic transport in both weakly and strongly modulated 1D antidot arrays defined in a narrow 2DEG constriction. In particular, we are concerned about the miniband and minigap structures of the antidot arrays and the effect of wave interferences on electron transport in the systems. We will explore them by computing the conductance of the systems as a function of the Fermi energy E_F.

II. FORMALISM

Let us consider a lateral ballistic constriction of width w_c having electrons confined along the y direction but allowed to move along the x direction, and being connected with two perfect semi-infinitely long leads with equal Fermi energy and with widths w_L and w_R, respectively. Without loss of generality, we assume that $w_L = w_R = w$ with $w \geq w_c$. When a potential difference is applied, the two perfect leads will serve as the reservoirs of emitter and collector. We further assume that the lateral quantum constriction can be divided along the longitudinal x direction into transverse strips, which are thin enough so that the potential in each strip region is of transverse y-direction dependence only. This is illustrated in Fig. 1 where the quantum constriction has been partitioned into N transverse strips. The Schödinger equation of motion of an electron with energy ε in the transverse strip region i can then be written as

$$\left[-\frac{\hbar^2}{2m^*}\left(\frac{\partial^2}{\partial x^2}+\frac{\partial^2}{\partial y^2}\right)+V_c(y)+V_b^i(y)\right]\Psi^i(x,y) = \varepsilon\Psi^i(x,y) , \quad (1)$$

where m^* is the effective mass, the confinement potential $V_c(y)$ is zero inside the constriction and infinite outside, and $V_b^i(y)$ describes the electron potential in the strip region. Expanding the wave function $\Psi^i(x,y)$ in terms of the transverse eigenstates $\{\Phi_n(y)\}$ of the two perfect leads with eigenvalues $\{\varepsilon_n\}$ gives

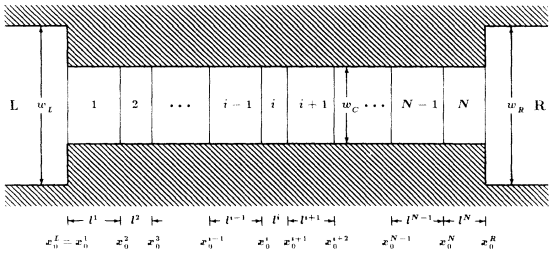

FIG. 1. Schematic representation of a finite 2DEG constriction of width w_c in which the electron potential varies along both the transportation x and the transverse y directions. The constriction is connected with two perfect semi-infinitely long 2DEG leads with equal Fermi energy and with widths w_L and w_R, respectively. We assume that $w_L = w_R = w$ with $w \geq w_c$ and that when a potential difference is applied electrons flow from L to R. The constriction is partitioned into N transverse strips in such a way that in each strip the electron potential varies only along the transverse y direction.

$$\Psi^i(x,y) = \sum_n \Phi_n(y) \sum_\alpha d_{n\alpha}^i \left[b_\alpha^i e^{ik_\alpha^i(x-x_0^i)} + c_\alpha^i e^{-ik_\alpha^i(x-x_0^i)}\right] , \quad (2)$$

where x_0^i is the reference coordinate along the x direction for the strip region i and has been specified in Fig. 1, $d_{n\alpha}^i$ are the expansion coefficients obtained by searching for eigenvalues E_α^i from the system

$$\sum_m \{(\varepsilon_n - E_\alpha^i)\delta_{nm} + \langle \Phi_n(y)|V_c(y)+V_b^i(y)|\Phi_m(y)\rangle\} d_{m\alpha}^i = 0, \quad n = 1,2,3,\ldots . \quad (3)$$

The quantity k_α^i can be expressed in terms of E_α^i and the energy ε of the electron injected into the region,

$$k_\alpha^i = \left[\frac{2m^*(\varepsilon - E_\alpha^i)}{\hbar^2}\right]^{1/2} . \quad (4)$$

We note that for a fixed ε the quantity k_α^i can be either real or imaginary, and we use the convention $(-1)^{1/2} = i$ when k_α^i is imaginary.

Obviously, we have a set of unknown coefficients b_α^i and c_α^i in the expansion of the wave function $\Psi^i(x,y)$ in each transverse strip region. However, the connection between the coefficients in any two transverse strip regions in the constriction can be achieved by a matrix method. In the transfer-matrix method, the expansion coefficients b_α^i and c_α^i in the strip region i and the expansion coefficients b_α^{i+1} and c_α^{i+1} in the strip region $i+1$ are related by a transfer matrix $\mathbf{M}(i,i+1)$,

$$\begin{bmatrix}\mathbf{B}^i \\ \mathbf{C}^i\end{bmatrix} = \mathbf{M}(i,i+1)\begin{bmatrix}\mathbf{B}^{i+1} \\ \mathbf{C}^{i+1}\end{bmatrix} \equiv \begin{bmatrix}\mathbf{M}_{11}(i,i+1) & \mathbf{M}_{12}(i,i+1) \\ \mathbf{M}_{21}(i,i+1) & \mathbf{M}_{22}(i,i+1)\end{bmatrix}\begin{bmatrix}\mathbf{B}^{i+1} \\ \mathbf{C}^{i+1}\end{bmatrix} , \quad (5)$$

where $\mathbf{B}^i$ and $\mathbf{C}^i$ are coefficient vectors containing $\{b_\alpha^i\}$ and $\{c_\alpha^i\}$, respectively. It has been derived in Refs. 9 and 10 that the transfer matrix $\mathbf{M}(i,i+1)$ can be written as

$$\mathbf{M}(i,i+1) = \begin{bmatrix}\gamma^i & 0 \\ 0 & (\gamma^i)^{-1}\end{bmatrix}^{-1} \mathbf{T}(i,i+1) , \quad (6)$$

where γ^i is the diagonal matrix with elements given by

$$(\gamma^i)_{\alpha\alpha} = \exp(ik_\alpha^i l^i) , \quad (7)$$

and $\mathbf{T}(i,i+1)$ is the matrix defined by

$$\mathbf{T}(i,i+1) = \begin{bmatrix}\mathbf{P}^i & \mathbf{P}^i \\ \mathbf{Q}^i & -\mathbf{Q}^i\end{bmatrix}^{-1}\begin{bmatrix}\mathbf{P}^{i+1} & \mathbf{P}^{i+1} \\ \mathbf{Q}^{i+1} & -\mathbf{Q}^{i+1}\end{bmatrix} , \quad (8)$$

with the submatrices $\mathbf{P}^i$ and $\mathbf{Q}^i$ given by

$$(\mathbf{P}^i)_{n\alpha} = d_{n\alpha}^i, \quad (\mathbf{Q}^i)_{n\alpha} = d_{n\alpha}^i k_\alpha^i w . \quad (9)$$

Here l^i is the width of the ith transverse strip region along the x direction and we recall that w is the width of the two perfect leads (see Fig. 1). Explicitly, the submatrices of $\mathbf{M}(i,i+1)$ are

$$\begin{aligned}
\mathbf{M}_{11}(i,i+1)&=(\gamma^i)^{-1}\mathbf{T}_{11}(i,i+1)\ ,\\
\mathbf{M}_{12}(i,i+1)&=(\gamma^i)^{-1}\mathbf{T}_{12}(i,i+1)\ ,\\
\mathbf{M}_{21}(i,i+1)&=\gamma^i\mathbf{T}_{21}(i,i+1)\ ,\\
\mathbf{M}_{22}(i,i+1)&=\gamma^i\mathbf{T}_{22}(i,i+1)\ .
\end{aligned}\tag{10}$$

The connection between the expansion coefficients of the electron wave function in the two perfect leads is

$$\begin{bmatrix}\mathbf{B}^L\\ \mathbf{C}^L\end{bmatrix}=\mathbf{M}(L,R)\begin{bmatrix}\mathbf{B}^R\\ \mathbf{C}^R\end{bmatrix}\ ,\tag{11}$$

where $\mathbf{B}^L$ and $\mathbf{C}^L$ are the coefficient vectors containing $\{b_\alpha^L\}$ and $\{c_\alpha^L\}$, $\mathbf{B}^R$ and $\mathbf{C}^R$ are the coefficient vectors containing $\{b_\alpha^R\}$ and $\{c_\alpha^R\}$, and $\mathbf{M}(L,R)$, is the total transfer matrix of the system given by

$$\mathbf{M}(L,R)=\mathbf{M}(L,1)\times\prod_{i=1}^{N-1}\mathbf{M}(i,i+1)\times\mathbf{M}(N,R)\ ,\tag{12}$$

where $\mathbf{M}(L,1)$ and $\mathbf{M}(N,R)$ are the two transfer matrices that couple the wave function in the quantum constriction to the wave function in the two perfect leads. These two matrices are not directly defined in Eqs. (6) and (10). However, a derivation of these two matrices can be found in Appendix A.

It is seen from Eq. (10) that both γ^i (forward states) and $(\gamma^i)^{-1}$ (backward states) are present in the transfer matrix $\mathbf{M}(i,i+1)$. The elements of the matrix $\mathbf{T}(i,i+1)$ depend closely on the basis on which the transverse modes in the strip regions i and $i+1$ have been expanded, while the elements of the matrix γ^i do not. The matrix γ^i will always appear in the formulation as the diagonal matrix given by Eq. (7). The elements $(\gamma^i)_{\alpha\alpha}$ of the matrix can be either purely real or complex. For a propagating mode α, where k_α^i is real, $(\gamma^i)_{\alpha\alpha}$ is, in general, to be a complex number with $|(\gamma^i)_{\alpha\alpha}|=1$ and thus carries the phase shift of the forward wave of the propagating mode. $[(\gamma^i)_{\alpha\alpha}^{-1}$ carries the phase shift of the backward wave of the propagating mode.] For an evanescent mode, where k_α^i becomes imaginary, the $(\gamma^i)_{\alpha\alpha}$ and $(\gamma^i)_{\alpha\alpha}^{-1}$ will, respectively, decay and grow exponentially. The presence of both these very fast growing and these very fast decaying terms in the transfer matrix $\mathbf{M}(i,i+1)$ is the cause of the numerical problem with the transfer-matrix technique. In fact, this has been known and understood for quite some time for layered 1D systems, as discussed by Ko and Inkson.[12] However, this origin of the problem has not been explicitly shown, previously, for multidimensional systems such as laterally confined and patterned 2DEG's. In our early calculations,[9,10] we found that the transfer-matrix method is numerically unstable for lateral systems, unless a rather weak modulation potential and/or an overall short quantum constriction are considered.

This numerical instability may be removed from the calculations by reformulating the problem with use of the scattering-matrix method.[12] The essence of the method is to separate the forward and backward states included in the description of the wave function of a quantum system and to let the less localized propagating modes rather than the evanescent modes dominate numerically. This is realized by coupling explicitly the outgoing state vectors $\mathbf{B}^R$ and $\mathbf{C}^L$ to the incoming state vectors $\mathbf{B}^L$ and $\mathbf{C}^R$ of the system via the scattering matrix $\mathbf{S}(L,R)$

$$\begin{aligned}\begin{bmatrix}\mathbf{B}^R\\ \mathbf{C}^L\end{bmatrix}&=\mathbf{S}(L,R)\begin{bmatrix}\mathbf{B}^L\\ \mathbf{C}^R\end{bmatrix}\\ &\equiv\begin{bmatrix}\mathbf{S}_{11}(L,R) & \mathbf{S}_{12}(L,R)\\ \mathbf{S}_{21}(L,R) & \mathbf{S}_{22}(L,R)\end{bmatrix}\begin{bmatrix}\mathbf{B}^L\\ \mathbf{C}^R\end{bmatrix}\ .\end{aligned}\tag{13}$$

Similarly, we may define the scattering matrix $\mathbf{S}(L,i)$ for the subsystem up to the ith transverse strip region through the equation

$$\begin{aligned}\begin{bmatrix}\mathbf{B}^i\\ \mathbf{C}^L\end{bmatrix}&=\mathbf{S}(L,i)\begin{bmatrix}\mathbf{B}^L\\ \mathbf{C}^i\end{bmatrix}\\ &\equiv\begin{bmatrix}\mathbf{S}_{11}(L,i) & \mathbf{S}_{12}(L,i)\\ \mathbf{S}_{21}(L,i) & \mathbf{S}_{22}(L,i)\end{bmatrix}\begin{bmatrix}\mathbf{B}^L\\ \mathbf{C}^i\end{bmatrix}\ .\end{aligned}\tag{14}$$

With the help of the transfer matrix $\mathbf{M}(i,i+1)$ defined in Eq. (5), an iterative relation for the scattering matrix $\mathbf{S}(L,i+1)$ of the subsystem up to the $(i+1)$th transverse strip region can be derived (see Appendix B). The submatrices of the scattering matrix $\mathbf{S}(L,i+1)$ are given by

$$\begin{aligned}
\mathbf{S}_{11}(L,i+1)&=[1-\mathbf{M}_{11}^{-1}(i,i+1)\mathbf{S}_{12}(L,i)\\
&\quad\times\mathbf{M}_{21}(i,i+1)]^{-1}\mathbf{M}_{11}^{-1}(i,i+1)\mathbf{S}_{11}(L,i)\ ,\\
\mathbf{S}_{12}(L,i+1)&=[1-\mathbf{M}_{11}^{-1}(i,i+1)\mathbf{S}_{12}(L,i)\mathbf{M}_{21}(i,i+1)]^{-1}\\
&\quad\times[\mathbf{M}_{11}^{-1}(i,i+1)\mathbf{S}_{12}(L,i)\mathbf{M}_{22}(i,i+1)\\
&\quad-\mathbf{M}_{11}^{-1}(i,i+1)\mathbf{M}_{12}(i,i+1)]\ ,\\
\mathbf{S}_{21}(L,i+1)&=\mathbf{S}_{22}(L,i)\mathbf{M}_{21}(i,i+1)\mathbf{S}_{11}(L,i+1)\\
&\quad+\mathbf{S}_{21}(L,i)\ ,\\
\mathbf{S}_{22}(L,i+1)&=\mathbf{S}_{22}(L,i)\mathbf{M}_{21}(i,i+1)\mathbf{S}_{12}(L,i+1)\\
&\quad+\mathbf{S}_{22}(L,i)\mathbf{M}_{22}(i,i+1)\ .
\end{aligned}\tag{15}$$

Thus, by knowing the scattering matrix $\mathbf{S}(L,1)$, we may calculate all the successive scattering matrices $\mathbf{S}(L,2)$, $\mathbf{S}(L,3),\ldots,\mathbf{S}(L,N)$ with use of Eq. (15). The scattering matrix $\mathbf{S}(L,R)\equiv\mathbf{S}(L,N+1)$ is then calculated by letting $i=N$ and $\mathbf{M}(N,N+1)\equiv\mathbf{M}(N,R)$. The initial scattering matrix $\mathbf{S}(L,1)$ can be obtained from Eq. (15) by letting $i=0$, $\mathbf{M}(0,1)\equiv\mathbf{M}(L,1)$, and $\mathbf{S}(L,0)\equiv\mathbf{S}(L,L)$ with use of the fact that $\mathbf{S}(L,L)=1$ (see Appendix A).

The stability of the scattering-matrix method is derived from the separation of the forward and backward states and the conversion of the matrix $(\gamma^i)^{-1}$ corresponding to the backward states appeared in the transfer matrix $\mathbf{M}(i,i+1)$ into the matrix γ^i corresponding to the forward states, and from the cancellation of $(\gamma^i)^{-1}$ with (γ^i) in the formalism. This may be seen by closely looking at Eqs. (10) and (15). In Eq. (15), the submatrices $\mathbf{M}_{11}(i,i+1)$ and $\mathbf{M}_{12}(i,i+1)$ appear as the forms of $\mathbf{M}_{11}^{-1}(i,i+1)$ and of $\mathbf{M}_{11}^{-1}(i,i+1)\mathbf{M}_{12}(i,i+1)$. Using Eq. (10), we immediately obtain that $\mathbf{M}_{11}^{-1}(i,i+1)=\mathbf{T}_{11}^{-1}(i,i+1)\gamma^i$, by which $(\gamma^i)^{-1}$ has been converted

into γ^i, and that $\mathbf{M}_{11}^{-1}(i,i+1)\mathbf{M}_{12}(i,i+1)=\mathbf{T}_{11}^{-1}(i,i+1)\mathbf{T}_{12}(i,i+1)$, i.e., the cancellation of $(\gamma^i)^{-1}$ with γ^i has been achieved. For evanescent modes, the corresponding elements of γ^i decay exponentially. Thus, as we expected, those elements of γ^i originating from the propagating modes become dominant in the calculations for the scattering matrices.

A unique solution of the Schrödinger equation of the quantum system can be obtained only after we impose a boundary condition on the electron wave function. Here we are interested in such electron states that may carry the electric current through the quantum system. Thus, let us consider an electron in the left lead in a state, $\Phi_m(y)e^{ik_m(x-x_0^L)}$, propagating forward from left to right with energy ε and wave vector $k_m=[2m^*(\varepsilon-\varepsilon_m)/\hbar^2]^{1/2}$, where ε_m is the eigenenergy of the transverse eigenstate $\Phi_m(y)$. After being scattered in the patterned quantum constriction, the wave function of the electron in the left and right leads should be written, in terms of the transverse eigenstates $\{\Phi_n(y)\}$, respectively, as

$$\Psi^L(x,y)=\Phi_m(y)e^{ik_m(x-x_0^L)}+\sum_n \Phi_n(y)\sum_\alpha d_{n\alpha}^L c_\alpha^L e^{-ik_\alpha^L(x-x_0^L)}, \tag{16}$$

$$\Psi^R(x,y)=\sum_n \Phi_n(y)\sum_\alpha d_{n\alpha}^R b_\alpha^R e^{ik_\alpha^R(x-x_0^R)}. \tag{17}$$

Thus, the boundary condition imposed on the wave function of the electron is

$$\begin{bmatrix}\mathbf{B}^L\\ \mathbf{C}^R\end{bmatrix}=\begin{bmatrix}\mathbf{I}_m\\ \mathbf{0}\end{bmatrix}, \tag{18}$$

where $\mathbf{I}_m$ is a unit vector with elements given by $(\mathbf{I}_m)_\alpha=\delta_{\alpha m}$. Inserting this boundary condition into Eq. (13) gives

$$\begin{bmatrix}\mathbf{B}^R\\ \mathbf{C}^L\end{bmatrix}=\begin{bmatrix}\mathbf{S}_{11}(L,R) & \mathbf{S}_{12}(L,R)\\ \mathbf{S}_{21}(L,R) & \mathbf{S}_{22}(L,R)\end{bmatrix}\begin{bmatrix}\mathbf{I}_m\\ \mathbf{0}\end{bmatrix}. \tag{19}$$

The coefficient vectors $\mathbf{B}^R$ and $\mathbf{C}^L$ are then obtained from

$$\begin{aligned}\mathbf{B}^R&=\mathbf{S}_{11}(L,R)\mathbf{I}_m,\\ \mathbf{C}^L&=\mathbf{S}_{21}(L,R)\mathbf{I}_m.\end{aligned} \tag{20}$$

At $T=0$, the conductance of the quantum constriction in the linear-response regime can be written as

$$G=-\frac{em^*}{\pi\hbar^2}\sum_m^{(R)} J(E_F,k_m)/k_m, \tag{21}$$

where $J(E_F,k_m)$ is the current carried through the quantum system by the electron state associated with the incident wave $\Phi_m(y)e^{ik_m(x-x_0^L)}$ from left with energy E_F and wave vector $k_m=[2m^*(E_F-\varepsilon_m)/\hbar^2]^{1/2}$ (for a general derivation of the current $J(E_F,k_m)$, see Appendix C) and (R) indicates that the sum is taken over those values of m for which k_m is real. In terms of the expansion coefficients of the wave function in the perfect leads, the conductance is then simply given by

$$G=\frac{2e^2}{h}\sum_m^{(R)}\left[1-\sum_n^{(R)}\frac{k_n^L}{k_m}|c_n^L|^2\right]=\frac{2e^2}{h}\sum_m^{(R)}\sum_n^{(R)}\frac{k_n^R}{k_m}|b_n^R|^2. \tag{22}$$

Here, we wish to note that the method presented in this section is formulated in a basis of infinite order and is exact. However, Eq. (3) has to be solved numerically by truncating n and m at a high transverse level M. In the actual calculations we let M as large as it is necessary to obtain a desired convergence in the conductance. We further note that the method is also very general and has a large flexibility. The method can be easily used to treat electron transport in the quantum systems having very complicated structures in both the longitudinal and the transverse directions. We note also that in the calculation of the conductance, it is necessary to assume that the two perfect leads have a finite width w. This is because we would, otherwise, encounter a scattering matrix of infinite order, which cannot be handled numerically. We will show in the next section that the results of the calculations converge quickly as w increases, and in many cases such as antidot arrays all properties of interest can be obtained by simply setting w equal to the width w_c of the narrow constriction containing the structure of interest. Finally, we note that in this paper only the two mode-matching techniques, i.e., the transfer-matrix and the scattering-matrix methods, are discussed and compared. The recursive Green's function method[13] is in fact an alternative approach, which does not suffer from the numerical instability. Therefore, it would be very interesting to compare our calculation results with the calculations done by the recursive Green's function method. However, for the quantum systems as considered in this work, no such calculations are available and, therefore, the comparison cannot be made at the moment.

III. APPLICATION TO 1D ANTIDOT ARRAYS

For the demonstration of the power of the scattering-matrix method, we show in this section the results of the applications of the method to electron transport through 1D antidot arrays implanted in a 2DEG constriction. In addition, these antidot systems have their own transport properties of interest. The structure of our systems is depicted in Fig. 2(a), where the antidots have been modeled by squarelike potential barriers of size $l_x\times l_y$ and height V_b and have been placed, with an equal separation l_c, in the middle of the narrow constriction. In this work, the hard-wall confinements[14] have been assumed and the calculations have been performed with the assumption of an effective mass of $m^*=0.067m_e$, which is appropriate to the $Al_xGa_{1-x}As/GaAs$ interface. In the following, we will denote the width of the perfect leads as $w=w_L=w_R$ and the width of the constriction as w_c.

We have first applied our scattering-matrix formalism to an array of six weakly modulated antidots and have compared the results of this calculation with that of Ref. 9 obtained with the transfer-matrix technique. Figures 2(b) and 2(c) show the calculated conductance of the

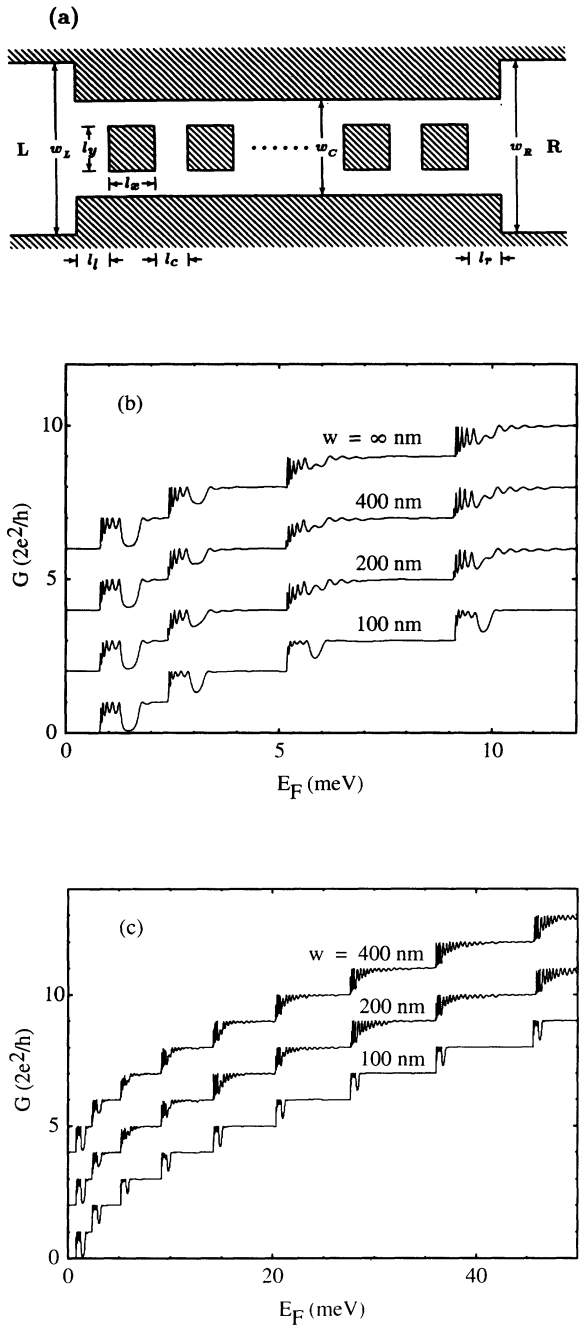

FIG. 2. (a) Schematic representation of the quantum system investigated in this work. N_d squarelike antidots with electron potential V_b and dimensions l_x and l_y are placed with an equal separation l_c in the middle of a narrow constriction of width w_c. The quantum system is connected with two perfect semi-infinitely long leads with widths w_L and w_R, respectively, and we assume that $w_L = w_R = w$ with $w \geq w_c$. (b) Calculated conductance G as a function of the Fermi energy E_F for the quantum system shown in (a) with six antidots ($N_d = 6$) and different lead width w. The geometrical parameters assumed in the calculations are $w_c = 100$ nm, $l_x = l_y = 50$ nm, $l_c = 40$ nm, $l_l = l_r = 30$ nm, and $V_b = E_1 \equiv (\hbar^2/2m^*)(\pi/w_c)^2$. The curves in the figure have been offset vertically for clarity. The curve for $w = \infty$ was obtained in Ref. 9 with the transfer-matrix method. (c) Same as (b), but for a larger range of the Fermi energy.

weakly modulated system with $l_x \times l_y = 50 \times 50$ nm^2 and $V_b = E_1 \equiv (\hbar^2/2m^*)(\pi/w_c)^2$ with $w_c = 100$ nm. The three lower curves are the results of the present calculations by the scattering-matrix method for $w = w_c$, $w = 2w_c$, and $w = 4w_c$, respectively, while the top curve is the result obtained previously by the transfer-matrix technique for $w = \infty$.[9] Overall, the same feature is seen in the calculated conductance traces for $w = 2w_c$, $w = 4w_c$, and $w = \infty$: Five sharp resonant peaks associated with the quasibound states localized in between the antidots appear at the edges of the conductance plateaus, and the plateaus are superimposed by oscillatory structures resulting from resonant tunneling through the longitudinal resonant states of the narrow constriction. By setting $w = w_c$, we see, in the lowest curve of Fig. 2(b), that these oscillatory structures are suppressed, but the five resonant peaks at the edges of the conductance plateaus remain. Figure 2(b) shows further that dips also appear in the calculated conductance traces. In the dimensions of antidots that we have assumed, the sharp resonant peaks are seen to be well separated by these dips from their adjacent conductance plateaus. In the limit case of an infinite number of antidots, the sharp resonant peaks should develop into electron miniband-associated conductance bands, while the dips develop into electron minigap-associated sharp conductance square wells.

With the transfer-matrix method, we could not investigate the electron transport for the systems with antidots either in large numbers or having a strong modulation potential, nor could we calculate the conductance at high Fermi energies even for the above system possessing only a small number of weakly modulated antidots. We can, however, fulfill these tasks quite easily with the scattering-matrix method. Figure 2(c) shows the calculated conductance by the scattering-matrix method for the same systems as for Fig. 2(b) but in a larger range of Fermi energies. We can see in this figure that for $V_b = E_1$, both the sharp resonant peaks and the dips are well preserved at high Fermi energies. This result may be seen more clearly in the lowest curve of Fig. 2(c) for which $w = w_c$ is assumed. In the cases of $w = 2w_c$ and $w = 4w_c$, large oscillatory structures are again seen to be superimposed on conductance plateaus at high Fermi energies.

Figure 3 shows the results of the scattering-matrix calculations for an array of 20 antidots with $V_b = E_1$ and three different values of $l_x \times l_y$. From now on, we will only consider the cases of $w = w_c$, in which the oscillatory structures at conductance plateaus are suppressed. For the array of antidots with $l_x \times l_y = 20 \times 20$ nm^2 (the lowest curve), we see that only shallow dips appear on the inside of the conductance plateaus at high Fermi energies. This may be as one expects, since such a small and weakly modulated potential should have rather small influences on the high-energy transverse modes of the narrow constriction. However, this potential may still be considered as a "strong" one for the low-energy transverse modes of the constriction. We see, for example, that sharp dips appear at the edges of the second and third conductance plateaus. These conductance dips can be well associated

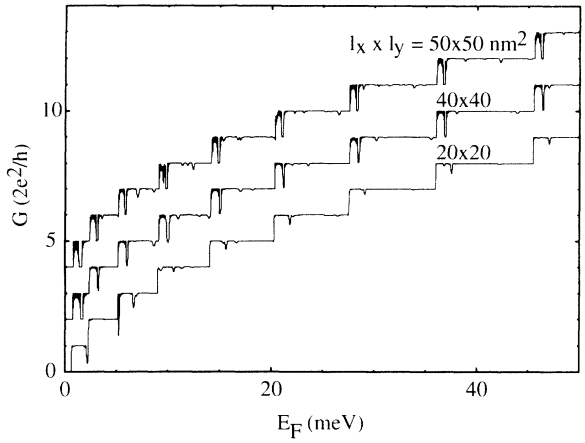

FIG. 3. Calculated conductance G as a function of the Fermi energy E_F for the quantum system in Fig. 2(a) with 20 weakly modulated antidots ($N_d=20$) of different dimensions $l_x \times l_y$. The geometrical parameters assumed in the calculations are $w=100$ nm, $w_c=100$ nm, $l_c=40$ nm, $l_l=l_r=30$ nm, and $V_b=E_1\equiv(\hbar^2/2m^*)(\pi/w_c)^2$. The curves in the figure have been offset vertically for clarity.

with the minigaps evolved from the 1D subbands of the narrow constriction. (For each transverse mode, the corresponding 1D subband will develop into minibands with minigaps in between under the influence of a periodic modulation potential, as we see in the electronic band structure of the 1D Kronig-Penney superlattice.) The sharp dip at the edge of the second conductance plateau can be attributed to the fact that the electron transport is blocked by the first minigap originated from the first 1D subband, while the sharp dip at the edge of the third conductance plateau to the fact that the electron transport is blocked by both the second minigap originated from the first 1D subband and the first minigap originated from the second 1D subband.

The top and middle curves of Fig. 3 show the calculated conductance for the array of antidots with $l_x \times l_y = 50 \times 50$ nm^2 and $l_x \times l_y = 40 \times 40$ nm^2, respectively. We note that the geometrical parameters of the antidots assumed in the calculation for the top curve of the figure is the same as for the lowest curve of Figs. 2(b) and 2(c). Comparing the top curve of Fig. 3 with the lowest curve of Fig. 2(c), we see that by increasing the number of the antidots in the array from 6 to 20 the dips at the edges of the conductance plateaus develop into conductance square wells of depth $2e^2/h$, indicating that the well-defined electronic minigaps are formed in the array of 20 antidots with $l_x \times l_y = 50 \times 50$ nm^2 and $V_b = E_1$. Such conductance square wells are also seen in the calculated conductance for the array of 20 antidots with $l_x \times l_y = 40 \times 40$ nm^2 and $V_b = E_1$ (see the middle curve of Fig. 3). In the top and middle curves of Fig. 3, we also see a rapidly oscillated conductance band before each electron minigap-associated conductance square well. As we mentioned before, this is due to the formation of the electron minibands from 1D subbands. All these results can be well understood by applying a simple 1D Kronig-Penney model to each transverse mode of the quantum systems under the adiabatic approximation.[15]

For a strong modulation potential, a complicated structure has been found in the calculated conductance of the antidot arrays. Figure 4 shows the calculated conductance for the array of 20 antidots with height $V_b = 1000$ meV. Figure 4(a) is for $l_x \times l_y = 20 \times 20$ nm^2, while Fig. 4(b) is for $l_x \times l_y = 40 \times 40$ nm^2. In both cases, strong conductance fluctuations, characterized by many broad dips and numerous sharp peaks, are seen over a large range of Fermi energies. However, conductance plateaus may still be recognized in the lower Fermi-energy region [i.e., at Fermi energies below 13.6 meV in Fig. 4(a) or below 24.0 meV in Fig. 2(b)], although these plateaus become piecewise due to the presence of many conductance gaps. Looking at the results in more details, we see in Fig. 4(b) two extremely narrow conductance

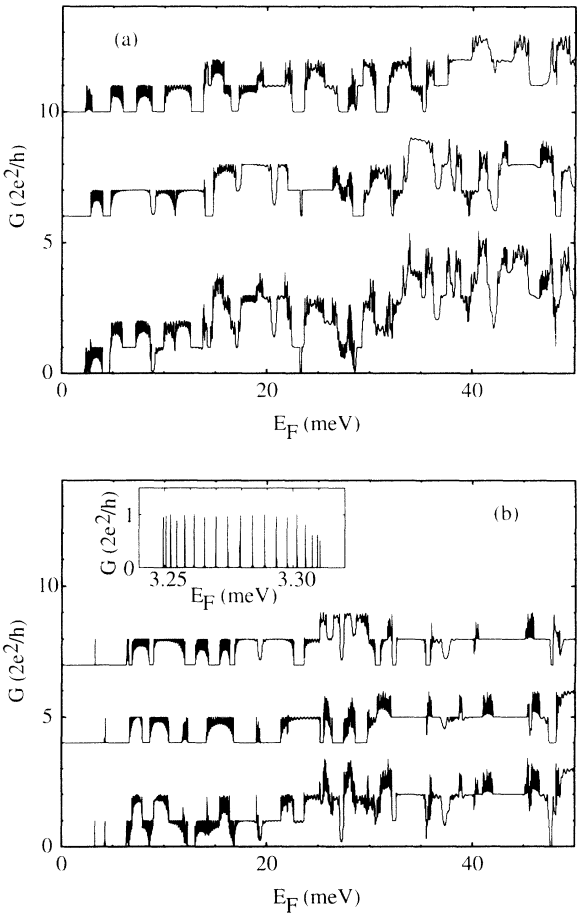

FIG. 4. (a) Calculated conductance G as a function of the Fermi energy E_F (bottom curve) for the quantum system shown in Fig. 2(a) with 20 strongly modulated antidots ($N_d=20$ and $V_b=1000$ meV) of dimensions $l_x \times l_y = 20 \times 20$ nm^2. The top curve shows the contribution to the conductance from the electron states of the even transverse parity, while the middle one shows that from the electron states of the odd transverse parity. The other geometrical parameters assumed in the calculations are $w=100$ nm, $w_c=100$ nm, $l_c=40$ nm, and $l_l=l_r=30$ nm. (b) Same as (a), but for $l_x \times l_y = 40 \times 40$ nm^2. The inset shows the extremely narrow conductance band at energies around 3.27 meV with refined Fermi energy.

bands. Each is composed of 19 sharp peaks [see the inset in Fig. 4(b) for the first one at energies around 3.27 meV]. Both of the conductance bands are located at energies well below the energy of the first 1D path of the antidot array and, therefore, correspond to electron transmission via resonant tunneling through the coupled quasibound states localized in between antidots. The first one is associated with the coupled quasibound states of even transverse parity, while the other one (at energies around 4.18 meV) is associated with the coupled quasibound states that have odd transverse parity. The two corresponding conductance bands are also observed in the array of the antidots of the smaller size [see Fig. 4(a)]. A difference in this case is that the two conductance bands are much wider and actually overlap to each other. This is simply because the interactions between the quasibound states in the array of the smaller antidots are much stronger.

After the first two 1D paths of the antidot arrays are energetically available for transmission, the conductance first shows a sharp increase to a value of $2\times(2e^2/h)$ and then a complicated structure characterized by fluctuations in high Fermi-energy range. Since the electron states of the different transverse parities do not interact, we may reduce the difficulty in our understanding of the results by considering the contributions to the conductance from the electron states of the even and odd parities separately. The top curves in Figs. 4(a) and 4(b) show the calculations for the even transverse parity, while the middle curves show that for the odd transverse parity. For each parity, a rather regular conductance-band structure can be seen when the Fermi energy is in between the energies of the first and second 1D paths of the parity. However, when we add the calculated results for the two different parities together to give the total conductance, a somewhat irregular behavior emerges. The conductance is seen to have a value close to $2\times(2e^2/h)$, when the transmission bands of the two different parities overlap or to have a value close to 0 when the transmission gaps of the two parities overlap. An irregular structure is also seen to appear in the calculated conductance for each parity at the Fermi energy higher than the energy of the second 1D path of the parity. Having in mind that in this case there are two or more energetically opened 1D paths, we may understand this irregular structure in the same way as above for the total conductance of the antidot array in the energy range where only the first even and the first odd paths of the array are open for transmission. By adding such already irregularly structured conductances of the different parities together, we should see a more complicated structure in the total conductance of the antidot arrays. It is more interesting to note that for the array of the smaller antidots ($l_x\times l_y=20\times20$ nm^2), rather strong fluctuations are seen in the calculated conductance at the Fermi energy higher than the energies of the third even and the third odd 1D paths of the antidot array. This high-energy conductance characteristic may also be understood, as above, as a result of mixing of the contributions from many different 1D paths. Such characteristic fluctuations should also be seen, but not shown in Fig. 4(b), in the calculated conductance for the array of the larger antidots ($l_x\times l_y=40\times40$ nm^2) after its third even and its third odd 1D paths are energetically open for transmission.

One other important feature of the strongly modulated antidot array is that in addition to the well-developed conductance square wells or gaps with the depths close to the multiples of $2e^2/h$, a number of dips with depth values different from the multiples of $2e^2/h$ are seen to appear in the calculated conductance traces. These dips can be understood as being due to wave interferences and will develop into conductance square wells or gaps as the number of antidots in the array is further increased. However, as long as a finite number of antidots are considered, such conductance dips should always appear. This finite-size effect may have to be taken into account in order to have a full understanding of transport measurements for an array of a finite number of strongly modulated antidots.

Overall, in the strongly modulated antidot array, we see an irregular conductance structure characterized by two kinds of fluctuations, namely slow and rapid fluctua-

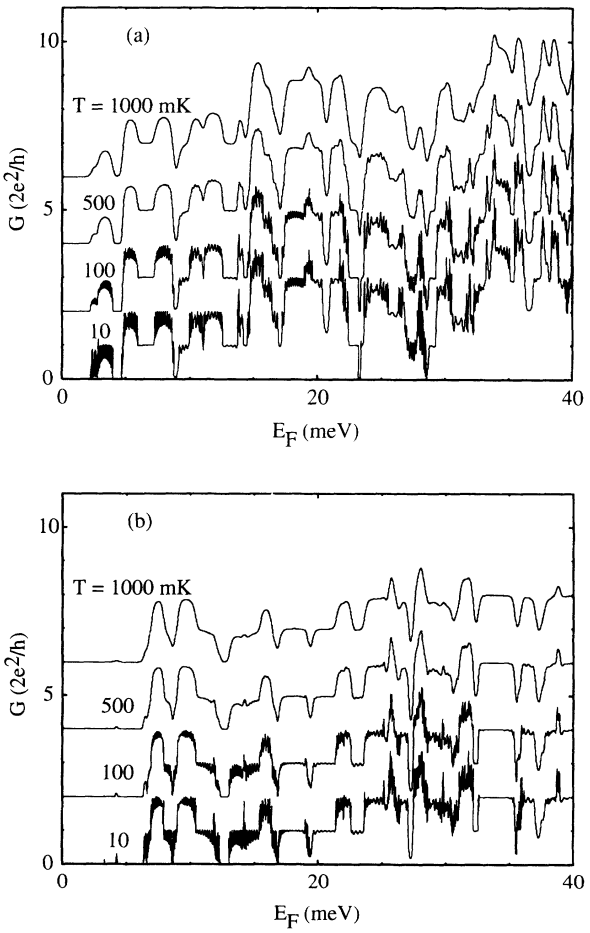

FIG. 5. Calculated conductance G as a function of the Fermi energy E_F at four finite temperatures for the same two strongly modulated antidot arrays ($N_d=20$ and $V_b=1000$ meV) as in Fig. 4, namely, all geometrical parameters of the array in (a) are the same as in Fig. 4(a) and that in (b) are the same as in Fig. 4(b).

tions, in the high Fermi-energy range. The slow fluctuations is associated with the effect of wave interferences and the formation of the electron minigaps in the array. This kind of fluctuation is insensitive to temperature up to a few Kelvin.[16] The conductance and resistance oscillations observed experimentally in Refs. 2 and 3 are examples of this kind of fluctuation. The rapid fluctuations can be traced to the formation of the electron minibands. However, due to the strong mixing of the contributions from different 1D paths in the array, the formation of regular electron minibands is only seen in the low Fermi-energy range. This kind of fluctuation can be easily smoothed out by thermal averaging and *ensemble* averaging, and may only be observed at very low temperature and the condition that the electron phase-coherence length is at least comparable with the sample dimension.[16] Only very recently has this kind of fluctuation been experimentally observed.[17] To give readers a rough feeling about up to what temperature the rapid conductance fluctuations can still be discernable, we plot finally in Fig. 5 the calculated conductance at four different finite temperatures[18] for the arrays of 20 strongly modulated antidots with the same geometrical parameters as in Fig. 4. Basically, there are no significant differences between the calculated conductance at $T=10$ mK and that at $T=0$ mK [see the lowest curves in Figs. 4(a) and 4(b) and in Figs. 5(a) and 5(b)]. The rapid fluctuations can still be seen at $T=100$ mK in the calculated conductance for the two strongly modulated antidot arrays and are well smoothed out at $T=500$ mK. However, the slow conductance fluctuations are seen to be well preserved at $T=1$ K [see the top curves in Figs. 5(a) and 5(b)].

IV. SUMMARY AND CONCLUDING REMARKS

We have presented a formulation of the scattering-matrix method for the calculation of electron transport through a lateral quantum system. Based on this formulation, we have shown explicitly that the less localized but physically important states are allowed to dominate in the calculations. As a consequence, the method remains numerically stable and accurate, even in the limit of strong modulations and consisting of a large number of quantum dots and antidots with large sizes. Thus, the problem of the numerical instability that one often encounters in the application of the transfer-matrix method to ballistic electron transport has been solved.

As an example of its application, the scattering-matrix method has been used to study electron transport in both weakly and strongly modulated 1D antidot arrays defined in a 2DEG constriction of width $w_c=100$ nm. In particular, we have been concerned about the electron miniband and minigap structures of the 1D arrays and the effect of wave interferences on electron transport in the systems. We have explored them by computing the conductance of the systems as a function of the Fermi energy E_F. For a weakly modulated antidot potential (i.e., $V_b \approx E_1$, where E_1 is the threshold energy of the 2DEG constriction for electron transmission), we have found that when the size of the antidots becomes large enough, the conductance bands, as a result of the formation of electron minibands, can appear at the edges of the conductance plateaus of the 2DEG constriction. This result agrees with our early calculation with the transfer-matrix method at low Fermi energies for an array of six antidots,[9] and has supplemented the result of that calculation at high Fermi energies and for the arrays with a larger number of antidots, i.e., in the situations where the transfer-matrix method fails. We argued that the electron miniband structure of the weakly modulated 1D antidot arrays can be well explained by applying a 1D Kronig-Penney model to each subband of the 2DEG constriction under the adiabatic approximation.

For the arrays with a strong modulation ($V_b \gg E_F$), we have seen a more complicated conductance structure. Two extremely narrow transmission bands have been found in the array of the 20 antidots of size $l_x \times l_y = 40 \times 40$ nm^2 at Fermi energies below the energies of the first even and the first odd 1D paths. These two conductance bands can be resolved into 19 peaks and can be attributed to resonant tunneling via the quasibound states localized in between the antidots. The two corresponding, but much wider, conductance bands can also be identified in the calculated conductance for the array of the 20 antidots of size $l_x \times l_y = 20 \times 20$ nm^2. In addition to these two conductance bands, the low Fermi-energy conductance of the strongly modulated antidot arrays is characterized by a piecewise plateau at a height close to $2 \times (2e^2/h)$ and gaps at a depth close to $2e^2/h$ or $2 \times (2e^2/h)$, reflecting the formation of many electron minibands and minigaps in the systems. At Fermi energies higher than the energies of the second even and the second odd 1D paths, the conductance of the antidot arrays shows strong fluctuations. This characteristic can be explained as a result of mixing of the contributions from many different 1D paths. Many dips with an irregular depth have been seen to appear over a large range of the Fermi energy in strongly modulated antidot arrays. These dips can be explained as an effect of wave interferences or, sometimes at high Fermi energies, as a mixing of the effect of wave interferences and the effect of the formation of the electron minigaps. Overall, we have shown, for the strongly modulated antidot arrays, that the conductance is characterized by two kinds of fluctuations, namely the slow and rapid fluctuations, in the high Fermi-energy range. The slow fluctuations result from wave interferences and the formation of the electron minigaps in the arrays, and are insensitive to temperature up to a few Kelvin, while the rapid fluctuations reflect the formation of the electron minibands and can be easily smoothed out by thermal averaging. Due to strong overlaps between the minibands associated with different 1D paths in the arrays, the regular miniband formation may only be observed in the low Fermi-energy range, even at very low temperature.

ACKNOWLEDGMENTS

The author is grateful to K.-F. Berggren, P. Omling, and L. Samuelson for many helpful suggestions and discussions. This work, which was performed within the nm-consortium in Lund, has been supported by the Swed-

ish National Science Research Council and the Swedish National Board for Industrial and Technical Development.

APPENDIX A: DERIVATION OF MATRICES $\mathbf{M}(L,1)$, $\mathbf{M}(N,R)$, and $\mathbf{S}(L,1)$

The following is a brief derivation of the transfer matrices $\mathbf{M}(L,1)$ and $\mathbf{M}(N,R)$ and the scattering matrix $\mathbf{S}(L,1)$. The transfer matrices $\mathbf{M}(L,1)$ and $\mathbf{M}(N,R)$ couple the wave function in the quantum channel to that in the two perfect leads. For the derivation of these two matrices, let us write the wave functions in the left and right leads, $\Psi^L(x,y)$ and $\Psi^R(x,y)$, in terms of the transverse eigenstates $\{\Phi_n(y)\}$ and eigenvalues $\{\varepsilon_n\}$ of the leads,

$$\Psi^L(x,y)=\sum_n \Phi_n(y)\sum_\alpha d_{n\alpha}^L[b_\alpha^L e^{ik_\alpha^L(x-x_0^L)} + c_\alpha^L e^{-ik_\alpha^L(x-x_0^L)}] \quad \text{(A1)}$$

$$\Psi^R(x,y)=\sum_n \Phi_n(y)\sum_\alpha d_{n\alpha}^R[b_\alpha^R e^{ik_\alpha^R(x-x_0^R)} + c_\alpha^R e^{-ik_\alpha^R(x-x_0^R)}] , \quad \text{(A2)}$$

where

$$d_{n\alpha}^L=d_{n\alpha}^R=\delta_{n\alpha} , \quad \text{(A3)}$$

$$k_\alpha^L=k_\alpha^R=k_\alpha=\left[\frac{2m^*(\varepsilon-\varepsilon_\alpha)}{\hbar^2}\right]^{1/2} . \quad \text{(A4)}$$

By matching $\Psi^L(x,y)$ to $\Psi^1(x,y)$ at $x=x_0^L=x_0^1$ and $\Psi^R(x,y)$ to $\Psi^N(x,y)$ at $x=x_0^R$, with the requirement that amplitudes and derivatives with respect to x are equal, we obtain

$$\mathbf{M}(L,1)=\mathbf{T}(L,1)\equiv\begin{bmatrix}\mathbf{P}^L & \mathbf{P}^L\\ \mathbf{Q}^L & -\mathbf{Q}^L\end{bmatrix}^{-1}\begin{bmatrix}\mathbf{P}^1 & \mathbf{P}^1\\ \mathbf{Q}^1 & -\mathbf{Q}^1\end{bmatrix} , \quad \text{(A5)}$$

$$\mathbf{M}(N,R)=\begin{bmatrix}\boldsymbol{\gamma}^N & \mathbf{0}\\ \mathbf{0} & (\boldsymbol{\gamma}^N)^{-1}\end{bmatrix}^{-1}\mathbf{T}(N,R) \equiv\begin{bmatrix}\boldsymbol{\gamma}^N & \mathbf{0}\\ \mathbf{0} & (\boldsymbol{\gamma}^N)^{-1}\end{bmatrix}^{-1} \times\begin{bmatrix}\mathbf{P}^N & \mathbf{P}^N\\ \mathbf{Q}^N & -\mathbf{Q}^N\end{bmatrix}^{-1}\begin{bmatrix}\mathbf{P}^R & \mathbf{P}^R\\ \mathbf{Q}^R & -\mathbf{Q}^R\end{bmatrix} , \quad \text{(A6)}$$

where $\boldsymbol{\gamma}^N$ can be calculated from Eq. (7), $\mathbf{P}^{1,N}$ and $\mathbf{Q}^{1,N}$ are obtained from Eq. (9), while $\mathbf{P}^{L,R}$ and $\mathbf{Q}^{L,R}$ are given by the following equation:

$$(\mathbf{P}^{L,R})_{n\alpha}=d_{n\alpha}^{L,R}=\delta_{n\alpha} ,$$
$$(\mathbf{Q}^{L,R})_{n\alpha}=d_{n\alpha}^{L,R}k_\alpha^{L,R}w=\delta_{n\alpha}k_\alpha w . \quad \text{(A7)}$$

The scattering matrix $\mathbf{S}(L,1)$ can be calculated from the transfer matrix $\mathbf{M}(L,1)$ as follows. Let us recall

$$\begin{bmatrix}\mathbf{B}^L\\ \mathbf{C}^L\end{bmatrix}=\mathbf{M}(L,1)\begin{bmatrix}\mathbf{B}^1\\ \mathbf{C}^1\end{bmatrix} \equiv\begin{bmatrix}\mathbf{M}_{11}(L,1) & \mathbf{M}_{12}(L,1)\\ \mathbf{M}_{21}(L,1) & \mathbf{M}_{22}(L,1)\end{bmatrix}\begin{bmatrix}\mathbf{B}^1\\ \mathbf{C}^1\end{bmatrix} \quad \text{(A8)}$$

and

$$\begin{bmatrix}\mathbf{B}^1\\ \mathbf{C}^L\end{bmatrix}=\mathbf{S}(L,1)\begin{bmatrix}\mathbf{B}^L\\ \mathbf{C}^1\end{bmatrix} \equiv\begin{bmatrix}\mathbf{S}_{11}(L,1) & \mathbf{S}_{12}(L,1)\\ \mathbf{S}_{21}(L,1) & \mathbf{S}_{22}(L,1)\end{bmatrix}\begin{bmatrix}\mathbf{B}^L\\ \mathbf{C}^1\end{bmatrix} . \quad \text{(A9)}$$

It is elementary to show

$$\begin{aligned}&\mathbf{S}_{11}(L,1)=\mathbf{M}_{11}^{-1}(L,1) ,\\ &\mathbf{S}_{12}(L,1)=-\mathbf{M}_{11}^{-1}(L,1)\mathbf{M}_{12}(L,1) ,\\ &S_{21}(L,1)=\mathbf{M}_{21}(L,1)\mathbf{M}_{11}^{-1}(L,1) ,\\ &\mathbf{S}_{22}(L,1)=-\mathbf{M}_{21}(L,1)\mathbf{M}_{11}^{-1}(L,1)\mathbf{M}_{12}(L,1)+\mathbf{M}_{22}(L,1) .\end{aligned} \quad \text{(A10)}$$

This result is identical to that obtained from Eq. (15) by letting $i=0$, $\mathbf{M}(0,1)\equiv\mathbf{M}(L,1)$, and $\mathbf{S}(L,0)\equiv\mathbf{S}(L,L)$ with the use of the fact that $\mathbf{S}(L,L)=1$.

APPENDIX B: DERIVATION OF AN ITERATIVE RELATION FOR SCATTERING MATRIX $\mathbf{S}(L,i+1)$

For the derivation of an iterative relation for scattering matrix $\mathbf{S}(L,i+1)$, let us recall the following two equations:

$$\begin{bmatrix}\mathbf{B}^i\\ \mathbf{C}^L\end{bmatrix}=\mathbf{S}(L,i)\begin{bmatrix}\mathbf{B}^L\\ \mathbf{C}^i\end{bmatrix} \equiv\begin{bmatrix}\mathbf{S}_{11}(L,i) & \mathbf{S}_{12}(L,i)\\ \mathbf{S}_{21}(L,i) & \mathbf{S}_{22}(L,i)\end{bmatrix}\begin{bmatrix}\mathbf{B}^L\\ \mathbf{C}^i\end{bmatrix} \quad \text{(B1)}$$

and

$$\begin{bmatrix}\mathbf{B}^i\\ \mathbf{C}^i\end{bmatrix}=\mathbf{M}(i,i+1)\begin{bmatrix}\mathbf{B}^{i+1}\\ \mathbf{C}^{i+1}\end{bmatrix} \equiv\begin{bmatrix}\mathbf{M}_{11}(i,i+1) & \mathbf{M}_{12}(i,i+1)\\ \mathbf{M}_{21}(i,i+1) & \mathbf{M}_{22}(i,i+1)\end{bmatrix}\begin{bmatrix}\mathbf{B}^{i+1}\\ \mathbf{C}^{i+1}\end{bmatrix} . \quad \text{(B2)}$$

By eliminating coefficient vectors $\mathbf{B}^i$ and $\mathbf{C}^i$ from the above two equations, we have

$$\begin{bmatrix}-\mathbf{S}_{22}(L,i)\mathbf{M}_{21}(i,i+1) & 1\\ \mathbf{M}_{11}(i,i+1)-\mathbf{S}_{12}(L,i)\mathbf{M}_{21}(i,i+1) & 0\end{bmatrix}\begin{bmatrix}\mathbf{B}^{i+1}\\ \mathbf{C}^L\end{bmatrix}=\begin{bmatrix}\mathbf{S}_{21}(L,i) & \mathbf{S}_{22}(L,i)\mathbf{M}_{22}(i,i+1)\\ \mathbf{S}_{11}(L,i) & \mathbf{S}_{12}(L,i)\mathbf{M}_{22}(i,i+1)-\mathbf{M}_{12}(i,i+1)\end{bmatrix}\begin{bmatrix}\mathbf{B}^L\\ \mathbf{C}^{i+1}\end{bmatrix} . \quad \text{(B3)}$$

The scattering matrix $\mathbf{S}(L,i+1)$ is then given by the rewriting the above equation as

$$\begin{bmatrix} \mathbf{B}^{i+1} \\ \mathbf{C}^{L} \end{bmatrix} = \begin{bmatrix} 0 & [\mathbf{M}_{11}(i,i+1)-\mathbf{S}_{12}(L,i)\mathbf{M}_{21}(i,i+1)]^{-1} \\ 1 & \mathbf{S}_{22}(\mathbf{L},i)\mathbf{M}_{21}(i,i+1)[\mathbf{M}_{11}(i,i+1)-\mathbf{S}_{12}(L,i)\mathbf{M}_{21}(i,i+1)]^{-1} \end{bmatrix}$$
$$\times \begin{bmatrix} \mathbf{S}_{21}(L,i) & \mathbf{S}_{22}(L,i)\mathbf{M}_{22}(i,i+1) \\ \mathbf{S}_{11}(L,i) & \mathbf{S}_{12}(L,i)\mathbf{M}_{22}(i,i+1)-\mathbf{M}_{12}(i,i+1) \end{bmatrix} \begin{bmatrix} \mathbf{B}^{L} \\ \mathbf{C}^{i+1} \end{bmatrix} \equiv \mathbf{S}(L,i+1) \begin{bmatrix} \mathbf{B}^{L} \\ \mathbf{C}^{i+1} \end{bmatrix} . \tag{B4}$$

After some elementary manipulations, the submatrices of the scattering matrix $\mathbf{S}(L,i+1)$, as shown in Eq. (15), are then derived.

APPENDIX C: CALCULATIONS OF THE ELECTRIC CURRENT $J(E_F,k_m)$

The electric current $J(E_F,k_m)$ carried through the quantum channel by the electron state associated with the incident wave $\Phi_m(y)e^{ik_m(x-x_0^L)}$ from left with energy E_F and wave vector $k_m=[2m^*(E_F-\varepsilon_m)/\hbar^2]^{1/2}$, can generally be expressed, in terms of the expansion coefficients of the wave function in any one of the transverse strip regions or in one of the two leads, as

$$J(E_F,k_m)=\frac{ie\hbar}{2m^*}\int_{-w/2}^{w/2}dy\left[\Psi_{k_m}^*(x,y)\frac{\partial}{\partial y}\Psi_{k_m}(x,y)-\Psi_{k_m}(x,y)\frac{\partial}{\partial y}\Psi_{k_m}^*(x,y)\right]$$
$$=-\frac{e\hbar}{2m^*}\sum_n\sum_{\alpha\beta}d_{n\alpha}d_{n\beta}^*\{(k_\alpha+k_\beta^*)[b_\alpha b_\beta^* e^{i(k_\alpha-k_\beta^*)(x-x_0)}-c_\alpha c_\beta^* e^{-i(k_\alpha-k_\beta^*)(x-x_0)}]$$
$$+(k_\alpha-k_\beta^*)[b_\alpha c_\beta^* e^{i(k_\alpha+k_\beta^*)(x-x_0)}-c_\alpha b_\beta^* e^{-i(k_\alpha+k_\beta^*)(x-x_0)}]\} . \tag{C1}$$

Here, the region index (i, L, or R) has been dropped, and the electron charge $-e$ has been assumed. This equation may be greatly simplified if we evaluate the current using the expansion coefficients of the wave function in a lead region. In the left lead, $d_{n\alpha}^L=\delta_{n\alpha}$ and $b_\alpha^L=\delta_{\alpha m}$, the current is then

$$J(E_F,k_m)=-\frac{e\hbar}{m^*}\left[k_m-\sum_n^{(R)}k_n^L|c_n^L|^2\right] , \tag{C2}$$

where (R) indicates that the sum is taken over those values of n for which $k_n^L=[2m^*(E_F-\varepsilon_n)/\hbar^2]^{1/2}$ is real. Similarly, in terms of the expansion coefficients of the wave function in the right lead, the current is

$$J(E_F,k_m)=-\frac{e\hbar}{m^*}\sum_n^{(R)}k_n^R|b_n^R|^2 . \tag{C3}$$

Combining Eqs. (C2) and (C3) gives the familiar relationship,

$$\sum_n^{(R)}(R_{mn}+T_{mn})\equiv\sum_n^{(R)}\left[\frac{k_n^L}{k_m}|c_n^L|^2+\frac{k_n^R}{k_m}|b_n^R|^2\right]=1 , \tag{C4}$$

where $R_{mn}=k_n^L/k_m|c_n^L|^2$ and $T_{mn}=k_n^R/k_m|b_n^R|^2$ are known as the reflection and the transmission coefficients, respectively.

[1]For a review, see C. W. J. Beenakker and H. van Houten, *Solid State Physics: Advances in Research and Applications,* edited by H. Ehrenreich and D. Turnbull (Academic, New York, 1991), Vol. 44, p. 1.

[2]K. Ismail, W. Chu, D. A. Antoniadis, and H. I. Smith, Appl. Phys. Lett. **52**, 1071 (1988).

[3]C. G. Smith, M. Pepper, R. Newbury, H. Ahmed, D. G. Hasko, D. C. Peacock, J. E. F. Frost, D. A. Ritchie, G. A. C. Jones, and G. Hill, J. Phys. Condens. Matter **2**, 3405 (1990).

[4]L. P. Kouwenhoven, F. W. J. Hekking, B. J. van Wees, C. J. P. M. Harmans, C. E. Timmering, and C. T. Foxon, Phys. Rev. Lett. **65**, 361 (1990).

[5]S. E. Ulloa, E. Castaño, and G. Kirczenow, Phys. Rev. B **41**, 12 350 (1990).

[6]J. A. Brum, Phys. Rev. B **43**, 12 082 (1991).

[7]Hua Wu, D. W. L. Sprung, J. Martorell, and S. Klarsfeld, Phys. Rev. B **44**, 6351 (1991).

[8]Hua Wu and D. W. L. Sprung, Phys. Rev. B **47**, 1500 (1993).

[9]Hongqi Xu, Zhen-Li Ji, and K.-F. Berggren, Superlatt. Microstruct. **12**, 237 (1992).

[10]Hongqi Xu, Phys. Rev. B **47**, 9537 (1993).

[11]For definition, see F. Merzbacher, *Quantum Mechanics* (Wiley, New York, 1970), Chap. 6, Sec. 6.

[12]D. Y. K. Ko and J. C. Inkson, Phys. Rev. B **38**, 9945 (1988).

[13]E. N. Economou and C. M. Soukoulis, Phys. Rev. Lett. **46**, 618 (1981); D. S. Fisher and P. A. Lee, Phys. Rev. B **23**, 6851 (1981); Phys. Rev. Lett. **47**, 882 (1981); L. Schweizer, B. Kramer, and A. MacKinnon, J. Phys. C **17**, 4111 (1984); Z. Phys. B **59**, 379 (1985); A. MacKinnon, *ibid.* **59**, 385 (1985).

[14]The hard-wall confinements may never be achieved experimentally, see, e.g., D. B. Chklovskii, B. I. Shklovskii, and L. I. Glazman, Phys. Rev. B **46**, 4026 (1992). However, in the linear ballistic transport regime, the detailed shape of the potential, which confines electrons to a 2DEG constriction, is not important in determining the fundamental physics of the system; see Ref. 1, and references cited therein.

[15]See, e.g., L. I. Glazman, G. B. Lesovik, D. E. Khmel'nitskii, and R. I. Shekhter, Pis'ma Zh. Eksp. Teor. Fiz. **48**, 218 (1988) [JETP Lett. **48**, 238 (1988)].

[16]Hongqi Xu (unpublished).

[17]R. Schuster, K. Ensslin, D. Wharam, S. Kühn, J. P. Kotthaus, G. Böhm, W. Klein, G. Tränkle, and G. Weimman, Phys. Rev. B **49**, 8510 (1994).

[18]For the derivation of the conductance at finite temperature see, e.g., Hongqi Xu, Phys. Rev. B **47**, 15 630 (1993).